Low-energy electron scattering from molecular hydrogen: Excitation of the $X\,^1\Sigma_g^+$ to $b\,^3\Sigma_u^+$ transition

M. Zawadzki,[1] R. Wright,[2] G. Dolmat,[2] M. F. Martin,[2] B. Diaz,[2] L. Hargreaves,[2] D. Coleman,[3] D. V. Fursa,[4] M. C. Zammit,[5] L. H. Scarlett,[4] J. K. Tapley,[4] J. S. Savage,[4] I. Bray,[4] and M. A. Khakoo[2,*]

[1]*Atomic Physics Division, Department of Atomic, Molecular, and Optical Physics, Faculty of Applied Physics and Mathematics, Gdańsk University of Technology, ulica Gabriela Narutowicza 11/12, 80-233 Gdańsk, Poland*

[2]*Department of Physics, California State University, Fullerton, California 92831, USA*

[3]*Department of Mechanical Engineering, California Polytechnic State University, San Luis Obispo, California 93407, USA*

[4]*Curtin Institute for Computation and Department of Physics and Astronomy, Curtin University, Perth, Western Australia 6102, Australia*

[5]*Theoretical Division, Los Alamos National Laboratory, Los Alamos, New Mexico 87545, USA*

(Received 1 September 2018; published 10 December 2018)

We present time-of-flight differential cross-section measurements and convergent close-coupling calculations of differential cross sections for the electron-impact excitation of the $X\,^1\Sigma_g^+ \rightarrow b\,^3\Sigma_u^+$ transition in molecular hydrogen. A part of this work was recently published [M. Zawadzki *et al.*, Phys. Rev. A **97**, 050702(R) (2018)]. In this work, agreement between theory and experiment is excellent overall, and marks a transition in electron-molecule scattering where differential scattering of excitation is found to be in such precise agreement. We also present total electron-impact excitation differential cross sections for H_2 for which agreement between theory and experiment is found to be excellent.

DOI: 10.1103/PhysRevA.98.062704

I. INTRODUCTION

The electron-impact excitation of molecular hydrogen counts as being the most significant problem in electron-molecule collisions. Molecular hydrogen is the simplest neutral molecular target and is abundant in astrophysical and planetary environments where electron-molecule excitation collisions play an important role in the production of observed photoemissions. Accurate collision data for molecular hydrogen are important for many applications ranging from astrophysics and fusion research [1] to material science and combustion physics [2]. For example, the modeling of stellar formation mechanisms [3] and strong H_2 emissions [4] of primordial gas clouds rely on the understanding of the nonequilibrium H_2 chemistry (production, destruction, cooling, and heating) of primordial gas clouds exposed to external ionizing radiation sources, where suprathermal secondary electrons are produced typically with energy in the range of 20–40 eV [4,5].

Due to the importance of e^--H_2 processes, Tawara *et al.* [6] published a detailed compilation of the available cross-section data regarding electron collisions with H_2 in 1990. In 2008 this list was updated by Yoon *et al.* [7] and a set of recommended cross sections was produced. The latter were predominantly compiled from available experimental data that were often few and in some cases had large uncertainties.

Considerable progress has been made regarding the electron-impact excitation of molecules, with theories such as the *R* matrix [8] and the Schwinger multichannel (SMC) model for a range of diatomic molecules such as H_2 [9] and N_2 [10], and polyatomic molecules such as H_2O [11] and thiophene (C_4H_4S) [12]. However, compared to electron collisions with atomic targets such as H, He, and alkali atoms, the situation for molecules (although impressive) is not at the same level of accuracy, simply because of the significantly greater complexity of molecular targets and the requirement of larger calculations to model electronic and nuclear structure and collision dynamics.

Molecular hydrogen, being the simplest neutral molecule, is the most amenable to detailed theoretical treatment. Nevertheless, the difficulty in taking into account all important reaction channels for collision systems lacking spherical symmetry proved to be formidable even without considering the need to include molecular vibrational and rotational degrees of freedom. Similar to the experimental electron-H_2 data set, only fragmentary theoretical electron-impact cross-section data were available, often with unqualified uncertainties and large discrepancies between various theoretical models and with experiment. This changed with the extension of the convergent close-coupling (CCC) method to electron collisions with molecules [13–15], and production of a comprehensive theoretical data set of accurate e^--H_2 cross sections [16–18]. A distinctive feature of the CCC cross-section data set was an explicit demonstration of convergence and an estimate of an accuracy of better than 11% for most transitions.

For many transitions and collision processes the CCC results [16,17] proved to be in significant disagreement with recommended cross sections. Particularly disturbing was the disagreement for electron-impact dissociation of H_2 into H atoms. This process was studied by Corrigan [19] in 1965, and is still the only experimental result available to date. His results essentially represent the sum of integral cross sections for the excitation of the triplet states of H_2 which decay into the $b\,^3\Sigma_u^+$ repulsive state together with cross sections for

*mkhakoo@fullerton.edu

various dissociation channels of the singlet states. Scarlett *et al.* [20] have used the CCC cross sections to model e^--H_2 dissociation into neutral fragments and found poor agreement with recommended dissociation cross sections [7] that were inferred from Corrigan's experiment.

The excitation of the $b\,^3\Sigma_u{}^+$ repulsive state that decays into $H(1^2S) + H(1^2S)$ ground state atoms is the major contribution to the recommended dissociation cross section. It is the most important dissociation pathway to forming atomic hydrogen atoms at low incident electron energies [20] and is of great importance in modeling gaseous environments such as astrophysical and industrial plasmas where molecular hydrogen is a substantial constituent. The CCC method [17] was used to calculate differential cross sections (DCSs) and integral cross sections (ICSs) for excitation of the $X\,^1\Sigma_g{}^+ \rightarrow b\,^3\Sigma_u{}^+$ transition of H_2. Recommended DCSs and ICSs for excitation of this transition were published by Yoon *et al.* [7] using measurements taken by several groups [21–24]. Zammit *et al.* [17] found that their ICSs were up to a factor of 2 smaller than the currently recommended data by Yoon *et al.* [7] at some incident electron energies (E_0). Most of these e^--H_2 measurements are more than 20 years old and were taken using conventional electrostatic electron spectrometers. Clearly, there is a case for a careful look at e^--H_2 collisions using new and improved experimental techniques and establishing new benchmarks with the aim of verifying the CCC cross sections or other models and guiding future developments of theoretical methods.

Accurate elastic scattering DCS measurements are available [25–29] using electron energy-loss spectroscopy methods coupled with the relative flow method [25], and the CCC method has shown excellent agreement particularly with those taken by our group [29]; see also Hargreaves *et al.* [30] where a comparison of this is made. However, inelastic H_2 DCSs are considerably more difficult to determine experimentally, because the molecular vibrational-electronic electron energy-loss features heavily overlap, and also in part the determination of the background under the extended $X\,^1\Sigma_g{}^+ \rightarrow b\,^3\Sigma_u{}^+$ continuum could not be properly accomplished in previous experiments. Recent measurements taken by our group [31] for the excitation of the $X\,^1\Sigma_g{}^+ \rightarrow B\,^1\Sigma_u{}^+$, $c\,^3\Pi_u$, $a\,^3\Sigma_g{}^+$, $C\,^1\Pi_u$, $E(F)\,^1\Sigma_g{}^+$ and $e\,^3\Sigma_u{}^+$ transitions further demonstrated improved agreement with the CCC results when compared to earlier theoretical models. An attempt to properly unfold the background-corrected spectra of H_2, in the energy-loss range of 11–13.5 eV by Hargreaves *et al.* [30] at E_0 values of 14–17.5 eV, i.e., lower than the E_0 values in [31], resulted in better agreement with the recent CCC model [16] for the excitation of the $X\,^1\Sigma_g{}^+ \rightarrow B\,^1\Sigma_u{}^+$, $c\,^3\Pi_u$, $a\,^3\Sigma_g{}^+$, $C\,^1\Pi_u$, and $E(F)\,^1\Sigma_g{}^+$ transitions, and provided a very good test of the CCC calculations, especially for the dipole-allowed $X\,^1\Sigma_g{}^+ \rightarrow B\,^1\Sigma_u{}^+$ and $C\,^1\Pi_u$ transitions.

In order to determine quantitative DCSs for (inelastic) excitation of electron energy-loss features, using electrostatic electron spectrometers, the energy-loss spectra are taken alongside the elastic scattering zero energy-loss feature in one spectrum. By normalizing the intensities of the inelastic features to the elastic feature, using generally available elastic DCSs, which are measured using the relative flow method [25,26] with a standard target (e.g., helium whose elastic DCSs have been accurately determined by experiments and theoretical models), inelastic DCSs for the inelastic features can be determined in a standard procedure. A significant systematic problem using this standard procedure, with electrostatic spectrometers, is in the characterization of the transmission of the electron scattering detector as a function of electron energy loss. This relative transmission T (usually normalized to the spectrometer's elastic peak response defined to be $= 1$) can be expressed as

$$T(E_0, E_L, \theta) = \left[\frac{I_s(E_0, E_L, \theta)}{I_s(E_0, 0, \theta)}\right] \Big/ \left[\frac{\mathrm{DCS}(E_0, E_L, \theta)}{\mathrm{DCS}(E_0, 0, \theta)}\right]. \tag{1}$$

T is an unknown function of E_0 and electron energy loss (E_L). T is found empirically to be weakly dependent on the electron scattering angle (θ) if the incident electron beam and the scattered electron detector are stable during the acquisition of angular scattering data. Here, $I_s(E_0, E_L, \theta)$ are the experimental electron scattering rates and $\mathrm{DCS}(E_0, E_L, \theta)$ are the actual DCSs for exciting features with E_L energy-loss values which are compared to DCSs for elastic scattering at $E_L = 0$ at the same E_0 and θ. A measurement of this transmission may be done using the energy-loss spectrum of helium (including the ionization continuum) at $E_0 \approx 30$ eV and $\theta = 90^\circ$ as was done by Pichou *et al.* [32] which was also implemented (with improved background correction) by our group in measuring the ionization doubly differential cross section for He [33].

A more precise, direct, and effective method of determining the spectrometer's transmission factor is using time-of-flight (TOF) elastic to inelastic DCS ratios as demonstrated in the TOF work of electrons scattering on N_2 by LeClair and Trajmar [34] at $\theta = 90^\circ$ or LeClair *et al.* [35] in He at $\theta = 90^\circ$. Their data enabled one to determine an average transmission over an extended E_L range, thus obtaining more accurate inelastic DCSs. TOF electron spectrometers do not have the fine energy resolutions of electrostatic electron spectrometers, but are able to detect different E_L electrons with uniform transmission and complement energy-loss spectrometers for quantitative determinations of inelastic electron scattering DCSs.

The instrument used by Le Clair and Trajmar [34] was a fixed-angle $\theta = 90^\circ$ detection device and a first operating TOF spectrometer, operating at a repetition rate of 100 kHz with the pulsed electrons produced by sweeping the unselected electron beam (0.5 eV energy resolution) across an aperture. However, their fixed θ limited the data that could be obtained. A later system capable of differential angles θ from 45° to 130°, with a higher energy resolution, energy-selected [60–80 meV, full width at half maximum (FWHM)] pulsed electron beam, was built by Buckman and co-workers [36] and was used to measure the excitation of He $n = 2, 3$ levels at $E_0 = 20.35$, 22.0, and 23.48 eV [37] as well as for Ar at 12.5, 14, 15, and 17.5 eV for θ from 55° to 125° [38] (see also [39]). Similarly as in [34] the beam was pulsed by sweeping it across an aperture, but at a higher 500 kHz rate. There is presently a paucity of differential TOF data for most atomic and molecular targets such as the rare gases, H_2, N_2, O_2, CO, H_2O, etc., for angles different from $\theta = 90^\circ$, which is needed to complement data taken by conventional electrostatic electron

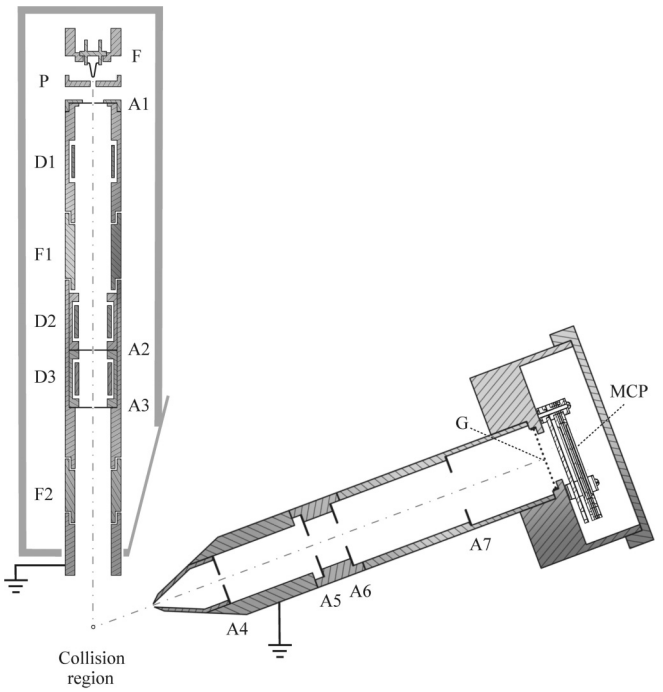

FIG. 1. Diagram of the experimental setup (not fully to scale at the anode region). TOF tube on lower right. Upper left, pulsed electron gun: F—electron filament; P—pulsed lens; A1—anode aperture; F1 and F2—focusing lenses; D1, D2 and D3 are electron deflector plates; A2, A3—object and pupil for collimating electron beam. Lower right, time-of-flight tube: A4–A7—molybdenum apertures; G—tungsten thin-wire square grid; MCP—*z*-stack [45] microchannel plate electron detector.

spectrometers. An immediately outstanding problem for such instruments is therefore the determination of excitation DCSs for H_2, especially the important $X\,^1\Sigma_g{}^+ \rightarrow b\,^3\Sigma_u{}^+$ transition.

With this H_2 $X\,^1\Sigma_g{}^+ \rightarrow b\,^3\Sigma_u{}^+$ transition problem in mind, we decided to build a differential scattering angle TOF electron spectrometer, and used it to determine excitation DCSs over an extended θ range from that of [34] or [36] for molecular targets and to first test the recent advances (see, e.g., [14–18]) of the CCC theory for H_2. The electron-impact excitation of the $b\,^3\Sigma_u{}^+$ state of H_2 is as fundamental a molecular process as the comparable atomic excitation of the $1S \rightarrow 2S$, $2P$ levels of hydrogen and must be measured to provide accurate tests of the present CCC cross sections.

II. EXPERIMENT

The present TOF system is different from other TOF setups in [34,36]. Here we aimed to get a more intense pulsed electron beam and to be able to detect scattered electrons over a much wider θ range. A detailed description of this device will be given in a methods paper to be published shortly, and consequently only the brief details are given. A schematic diagram of this instrument is given in Fig. 1. The electron beam is actuated by pulsing a 0.8-mm-thick (1 mm in diameter) lens (see P, Fig. 1) placed between the filament and anode using a 0–40-V, 0.5–8-ns pulse generator [40] wired in a 50-Ω impedance SMA rf coaxial cable circuit [41] using rf connectors and an rf 50-Ω terminating flange-type resistor screwed to the grounded box housing the electron gun and close to the aperture lens [42]. The shape of the exciting pulse is more of a triangular pulse than a square pulse. Therefore the exciting width of the pulse can be reduced by raising the negative dc bias on the lens so that only the "tip" of the waveform pulses on the electron beam. The TOF tube was made compact, but long (23.9 cm TOF distance, 3.3 cm inner diameter) and able to detect electrons from $\theta = 20^\circ$ to 135°. It was made of aluminum inside coated with sprayed, lightly colloidal graphite, but had a tapered nosepiece made of titanium, which had an opening of 2 mm (rather than 1 mm, so that it did not deflect slow electrons). The TOF tube had four tandem thin molybdenum apertures (0.07 mm thick), placed to subtend the same solid angle ($\approx 6^\circ$ FWHM) at the collision region and so to suppress secondary electrons (A4–A7, Fig. 1) reflected from the TOF tube body. This system (especially the opening 2-mm nose aperture) was heated by electrically shielded, biaxial, magnetically free heaters [43] to a temperature at first of 150 °C which was lowered to around 80 °C. The collision region was kept open and grounded. The electron beam current was measured by a flat molybdenum Faraday flag that was sooted and was rotated into place in the path of the electron beam to tune its intensity; the flag was removed to tune (focus) the scattering electron signal and allow collisions with the gas to take place. For the gas target source, we used an acetylene flame sooted molybdenum hypodermic needle 3 cm long and with an inner diameter of 0.8 mm incorporated into a movable source system developed in our laboratory [44] which accurately and expediently enabled the determination of scattering backgrounds. The detector was a triple microchannel plate system, 1 in. in diameter [45], whose front was biased at +300 V with respect to ground to provide an electron detection quantum efficiency that was independent of the incident kinetic energy of the detected electron. This potential was isolated from the grounded TOF tube using a single 95% transparency 2.5-mm-square, grounded tungsten grid [46] which was also sprayed lightly with colloidal graphite—chosen after a result of testing several other grid-type and slat-type setups that were used earlier (see, e.g., [34,36]).

The remanent B field was reduced to less than ±2 mG over a radius of *at least* 30 cm around the collision region using a set of vertical coils as well as a 1.25-mm-thick μ-metal shield with proper endcaps into the vacuum flanges [47], and it was only when this B field was finally reduced that the instrument began to work properly. Using a capacitively coupled positive-going pulse, 2–3 ns and 5–8 V in amplitude, and the pulsed aperture biased at a negative potential of −5 to −8 V, we were able to produce 1–5-μA peak current pulsed beams at a 500-kHz repetition rate, with pulse widths of ≈3 ns. The energy of the beam was determined accurately within ±0.2 eV using the TOF times of the $b\,^3\Sigma_u{}^+$ feature at 10.19 eV energy loss and the $C\,^1\Pi_u$ peak at 12.57 eV energy loss as well as the delay from prompt UV photons and the elastic peak. The "contact" potential (difference in the measured voltage between filament and collision region and the actual E_0 of the beam) was large and ranged from 4.5 to 5.5 eV which required the E_0 value of the gun to be calibrated for all fixed settings of the pulsed lens. This suggested that the pulse of electrons

selected emanated closer to the pulsed lens than the filament over a region of <1 mm. The gun had two ≈ 1 mm apertures to collimate the beam, with an angular spread of about 3° (FWHM). The sooted, molybdenum movable target needle was placed 6 mm below the center of the collision region to avoid electron scattering from it. The clean vacuum system was pumped by three 6-in. oil-free turbomolecular pumps, with a base pressure of around $\approx 1 \times 10^{-7}$ Torr or better with heater bakeouts fully on. The system was always vented to dry nitrogen and allowed to cool after which the vacuum chamber was opened for servicing to ensure cleanliness.

From a consideration of beam spreading from the filament region to the collision region, we estimate that the drift to the collision region added no more than 0.5 ns to the electron pulse. The electron temporal width was typically 2.8 ns for a pulsed beam with an average instantaneous current of about 2.5 nA. It could be reduced to less than 2 ns by lowering the pulse width or raising the dc bias on the pulsed aperture since, as stated before, the pulsed waveform was roughly triangular. Typical electron scattering signal rates were around 200 to >5000 Hz.

III. THEORY

The CCC method has been extensively applied to study electron and positron collisions with molecular hydrogen and its ion [15]. Cross sections for excitation of the $b\,^3\Sigma_u^+$ state of H_2 have been presented by Zammit *et al.* [17] within the fixed-nuclei (FN) approximation and were extended to lower excitation energies by Scarlett *et al.* [20] using the adiabatic nuclei (AN) approximation. Electron-impact excitation of the triplet $b\,^3\Sigma_u^+$ state from the singlet $X\,^1\Sigma_g^+$ ground state can occur only due to the electron exchange interaction and is strongly affected by interchannel coupling. Over the years there have been many theoretical methods applied to determine the $b\,^3\Sigma_u^+$ excitation cross section [8,9,48–54] which, however, showed little agreement with each other and with experiment, in particular for incident energies above 13 eV where a large number of other reaction channels become open and an accurate account of interchannel coupling becomes crucial.

The CCC calculations [17] have been performed in the FN approximation in a number of models, ranging from nine to 491 states. The target states used in these models are obtained via diagonalization of the H_2 Hamiltonian in a Sturmian (Laguerre) basis, which models all important reaction channels including ionization. For the small model (nine-state) the CCC results have shown a characteristic pseudoresonance behavior similar to previous theoretical results [55,56]. The converged cross sections have been established [17] by increasing the number of reaction channels and verifying the stability of the calculated cross sections. The CCC results proved to be in significant disagreement, in both the shape and absolute values, with the recommended $b\,^3\Sigma_u^+$ ICS [7] above 13 eV. The maximum of the recommended cross section at 15 eV was not supported by the CCC calculations, which predicted the maximum at 12 eV. Above 13 eV the disagreement in absolute values was as high as a factor of 2.

Accounting for nuclear motion becomes progressively more important as the incident electron energy becomes smaller. In the FN approximation the excitation threshold of the $b\,^3\Sigma_u^+$ state is at 10.31 eV at the average internuclear distance of $1.448\,a_0$ adopted in the FN CCC calculations [17]. The AN CCC approach [18] allows one to extend the theoretical technique to low excitation energies and proved to be in good agreement with the experiment for energies below 13 eV. The analysis of the CCC results has demonstrated that the nuclear motion effects are negligible above 14 eV verifying, therefore, the validity of the FN CCC results. Various tests have been performed to establish numerical stability of the obtained cross sections. The combined uncertainty of the CCC cross sections was estimated to be better than 11%.

The large disagreement between the CCC estimates of the $b\,^3\Sigma_u^+$ cross section and recommended values for such a fundamental reaction channel is of concern and requires a reanalysis of both theoretical and experimental techniques. A detailed analysis was conducted to test the theoretical results and it was concluded that the discrepancy between theory and experiment is unlikely to be due to the deficiencies in the theoretical treatment of the problem. A possibility for the experiment to overestimate the cross section for the $b\,^3\Sigma_u^+$ state excitation could in principle be due to the cascading from higher-lying triplet states. In fact, Scarlett *et al.* [20] have shown that the cascading contribution has a maximum at 16 eV and becomes larger than the direct $b\,^3\Sigma_u^+$ excitation cross section above 14 eV. However, the $b\,^3\Sigma_u^+$ DCS measurements [21–24] are cascade free; this, therefore, cannot explain the factor of 2 discrepancies between theory and experiment, and one must resort to a consideration of transmission and background scattering analysis in the experiments as causes of this difference.

IV. RESULTS AND DISCUSSION

A. Analysis of spectra

Figure 2 shows several TOF spectra for H_2 at $E_0 = 15$ eV taken at $\theta = 90°$. These spectra are obtained by subtracting the spectrum taken with the gas needle displaced away from the collision region (background scattering) from the corresponding spectrum taken with the needle aligned with the electron beam (signal plus background) [44], both taken alternately approximately every 600 s for a 7200–14 400 s acquisition time. From the background subtracted spectra we were able to determine accurate inelastic to elastic ratios (R) after removing an exponential contribution from the elastic peak's tail, which is produced by collisions of electrons with the gas and surfaces in the TOF tube [36]. Typical signal + background to background ratios were $\approx 2.5:1$, governed by the reduced pumping speed of our vacuum system of turbopumps for the light molecular mass H_2 as compared to N_2, etc. We also note that since the slower electrons are easier to deflect from the line of sight with the electron detector (by B fields significantly greater than a few mG and by dirt on the TOF tube optics), therefore in principle one expects that the higher the R value, the better is the measurement. We have taken TOF spectra at E_0 values of 9, 10, 11, 11.5, 12, 12.5, 13, 13.5, 14, 15, 15.5, 16, 17.5, 20, and 25 eV for θ of 20°–130°.

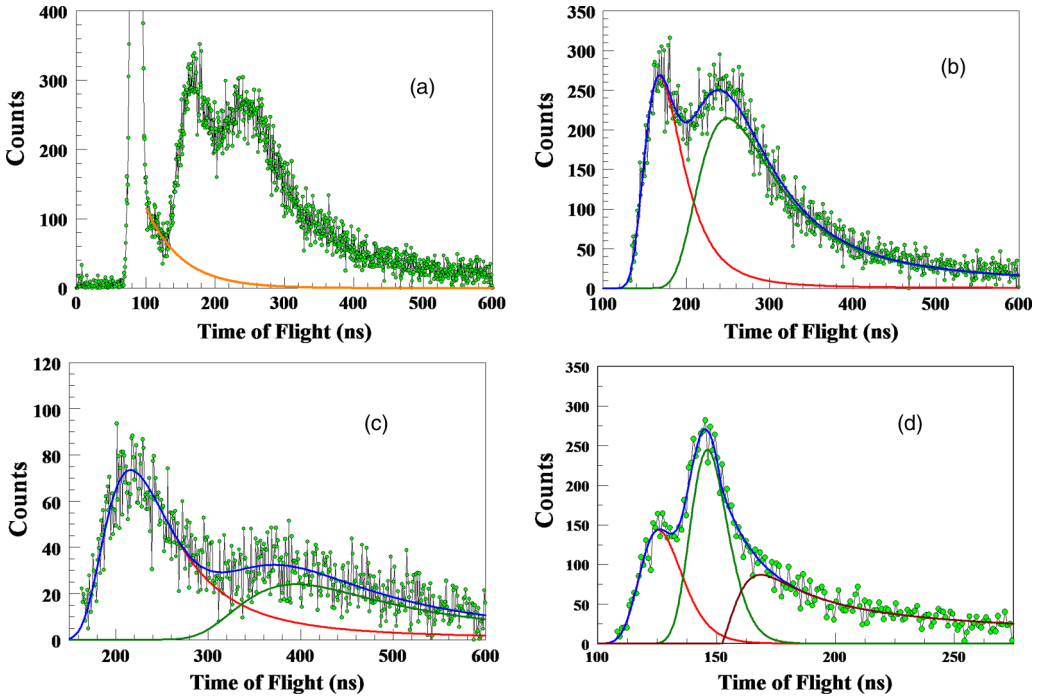

FIG. 2. (a) Background subtracted time-of-flight spectrum for electron scattering from H_2 taken at $E_0 = 15\,\text{eV}$ and $\theta = 90^\circ$ showing the elastic feature and the exponential tail of the elastic peak (orange line). (b) Inelastic part of (a) with exponential tail of elastic peak subtracted. The inelastic spectrum is fitted to the Franck-Condon envelope (red line) for the $X\,^1\Sigma_g{}^+ \rightarrow b\,^3\Sigma_u{}^+$ transition [22] and a function which represents the bound higher states of H_2 to fit the remaining spectrum [Eq. (2), green line], above the $b\,^3\Sigma_u{}^+$. Time is referenced relative to the crossing of the electron pulse over the collision region. The total fit is the blue line. (c) Time-of-flight spectrum similar to (b) taken at $E_0 = 13.5\,\text{eV}$ and $\theta = 90^\circ$ showing the increase of the $b\,^3\Sigma_u{}^+$ feature relative to the complete inelastic spectrum and (d) time-of-flight spectrum similar to (b) taken at $E_0 = 20\,\text{eV}$ and $\theta = 90^\circ$, showing the ionization continuum (fitted with the brown line). Other colored lines are the same as (b). See text for discussion.

At energies above the H_2 single-ionization potential of 15.43 eV [57], however, both target-ionized ejected electrons are detected as well as those projectile-scattered electrons after ionizing the target. Thus above $E_0 = 15.4\,\text{eV}$ the experimental ratios R presented are those which are a ratio of inelastically scattered projectile electrons, scattered from exciting bound states or ionizing the target *plus* electrons ejected for the ionization process to the vibrationally elastic scattered electrons. The CCC method, on the other hand, is able to distinguish both projectile-scattered electrons and ejected ionized electrons. Hence above the ionization threshold, measures must be taken to attempt to reconcile the present measured R values and the R values of the CCC calculations, which are a ratio of projectile inelastic plus ionization scattering DCS to the elastic scattering DCS. This process is elaborated on in Sec. IV E.

The elastic peak intensity was determined by integrating the counts under this feature. To determine the DCS for excitation of the $X\,^1\Sigma_g{}^+ \rightarrow b\,^3\Sigma_u{}^+$ transition, the TOF spectra were fitted to the Franck-Condon envelope of the $X\,^1\Sigma_g{}^+(v'' = 0) \rightarrow b\,^3\Sigma_u{}^+$ repulsive potential from Rescigno *et al.* [49] weighted by the flux factor k_f/k_i, where k_f is the scattered electron momentum and k_i is the incident electron momentum (see also [24,49]), in the TOF time coordinates and not energy-loss space. The remaining inelastic spectrum, excluding ionization, was approximated using a similar function for the $X\,^1\Sigma_g{}^+ \rightarrow b\,^3\Sigma_u{}^+$ feature:

$$f(t) = A \exp\left[-(\alpha/t^2 - \mu)/\sigma\right], \tag{2}$$

where the TOF is given by t, the intensity given by A, the scale time factor α (which is a numerical constant dependent on the timescale), the mean position is μ, and the width σ was nonlinearly fitted to the rest of the inelastic features. The sum of two fitting functions—for the $X\,^1\Sigma_g{}^+ \rightarrow b\,^3\Sigma_u{}^+$ state and the higher bound states of H_2—reproduced the inelastic transition features very well. To determine excitation DCSs (which do not include ionization) for energies above the ionization potential, the TOF spectrum was "cut off" at the ionization energy using a similar function as in Eq. (2) centered about the ionization TOF continuum. DCSs for the inelastic features were determined by normalizing the TOF spectrum intensity of the elastic scattering peak to our experimental DCSs of Muse *et al.* [29]. Tables I and II summarize our measured values of R and the determined DCSs for electron-impact excitation of the $X\,^1\Sigma_g{}^+ \rightarrow b\,^3\Sigma_u{}^+$ transition in H_2.

B. Inelastic to elastic ratios, *R*

Selected R values, which are relative measurements directly determined from our TOF spectra, (Table I) are plotted vs the CCC results in Fig. 3. Some of these have already been presented in an earlier Rapid Communication [58]. Initial trial

TABLE I. Inelastic to elastic ratios for H_2 from the TOF experiment with 1-standard-deviation errors.

E_0 (eV)→	9 eV		10 eV		11 eV		11.5 eV		12 eV		12.5 eV		13 eV		13.5 eV	
Angle (deg)↓	R	Error	R	Error	R	Error	R	Error	R	Error	R	Error	R	Error	R	Error
20	0.00178	0.00064	0.00121	0.00017	0.00536	0.00118	0.00298	0.00085	0.00870	0.00120	0.0128	0.0022	0.00585	0.00106	0.0171	0.0027
30	0.00196	0.00053	0.00236	0.00029	0.00542	0.00098	0.00527	0.00117	0.0110	0.0020	0.0130	0.0017	0.00817	0.00109	0.0181	0.0026
40	0.00287	0.00135	0.00361	0.00044	0.00891	0.00116	0.0103	0.0013	0.0128	0.0016	0.0175	0.0023	0.00697	0.00133	0.0212	0.0027
50	0.00409	0.00126	0.00545	0.00065	0.0123	0.0014	0.0187	0.0059	0.0169	0.0029	0.0268	0.0034	0.0100	0.0035	0.0273	0.0035
60	0.00382	0.00136	0.00806	0.00098	0.0166	0.0028	0.0245	0.0042	0.0255	0.0035	0.0381	0.0048	0.0244	0.0033	0.0406	0.0053
70	0.00579	0.00162	0.0125	0.0020	0.0305	0.0036	0.0430	0.0055	0.0388	0.0057	0.0583	0.0073	0.0424	0.0080	0.0744	0.0097
80	0.00641	0.00125	0.0210	0.0026	0.0465	0.0060	0.0535	0.0069	0.0549	0.0084	0.0974	0.0138	0.0534	0.0088	0.116	0.014
90	0.0109	0.0023	0.0287	0.0037	0.0778	0.0077	0.0849	0.0133	0.0851	0.0114	0.151	0.019	0.098	0.018	0.178	0.022
100	0.0144	0.0019	0.0440	0.0061	0.109	0.018	0.131	0.024	0.122	0.016	0.212	0.027	0.093	0.012	0.252	0.032
110	0.0171	0.0021	0.0630	0.0082	0.129	0.018	0.141	0.020	0.163	0.021	0.266	0.035	0.159	0.022	0.322	0.040
120	0.0223	0.0031	0.0775	0.0093	0.149	0.017	0.167	0.021	0.194	0.024	0.303	0.041	0.198	0.025	0.372	0.047
130	0.0245	0.0038	0.0891	0.0116	0.182	0.019	0.218	0.031	0.232	0.029	0.351	0.048	0.229	0.033	0.418	0.052
E_0 (eV)→	14 eV		14.5 eV		15 eV		15.5 eV		16 eV		17.5 eV		20 eV		25 eV	
Angle (deg)↓	R	Error	R	Error	R	Error	R	Error	R	Error	R	Error	R	Error	R	Error
20	0.0266	0.0038	0.0275	0.0038	0.0383	0.0060	0.0378	0.0048	0.0468	0.0057	0.0737	0.0096	0.147	0.019	0.316	0.040
30	0.0252	0.0038	0.0316	0.0045	0.0406	0.0053	0.0435	0.0067	0.0487	0.0072	0.0674	0.0109	0.112	0.019	0.262	0.035
40	0.0298	0.0045	0.0376	0.0049	0.0430	0.0060	0.0521	0.0066	0.0561	0.0075	0.0718	0.0114	0.131	0.019	0.241	0.030
50	0.0372	0.0055	0.0442	0.0058	0.0582	0.0104	0.0609	0.0077	0.0651	0.0085	0.0894	0.0204	0.140	0.024	0.260	0.033
60	0.0504	0.0064	0.0669	0.0084	0.0744	0.0091	0.0857	0.0125	0.0818	0.0114	0.126	0.016	0.164	0.021	0.326	0.039
70	0.0822	0.0107	0.0983	0.0131	0.0948	0.0118	0.115	0.018	0.126	0.017	0.166	0.021	0.247	0.030	0.413	0.050
80	0.140	0.019	0.161	0.021	0.152	0.020	0.183	0.023	0.188	0.023	0.251	0.039	0.336	0.043	0.578	0.079
90	0.214	0.032	0.248	0.031	0.254	0.032	0.261	0.034	0.277	0.038	0.316	0.041	0.461	0.056	0.745	0.091
100	0.317	0.040	0.331	0.057	0.341	0.045	0.371	0.047	0.398	0.049	0.488	0.084	0.599	0.072	0.893	0.121
110	0.391	0.058	0.422	0.075	0.459	0.055	0.443	0.090	0.503	0.067	0.660	0.083	0.731	0.091	1.03	0.15
120	0.438	0.062	0.462	0.073	0.536	0.068	0.549	0.069	0.617	0.076	0.774	0.098	0.838	0.101	1.23	0.15
130	0.486	0.061	0.541	0.099	0.623	0.076	0.616	0.077	0.682	0.084	0.893	0.113	0.991	0.120	1.48	0.18

TABLE II. DCSs (units of a_0^2) for excitation of the $X\,^1\Sigma_g^+ \rightarrow b\,^3\Sigma_u^+$ transition in H_2 determined from our TOF spectra, with 1-standard-deviation errors. Values in italics are extrapolated values used to determine ICSs.

E_0 (eV)→	9 eV		10 eV		11 eV		11.5 eV		12 eV		12.5 eV		13 eV		13.5 eV	
Angle (deg)↓	DCS	Error	DCS	Error	DCS	Error	DCS	Error	DCS	Error	DCS	Error	DCS	Error	DCS	Error
0	*0.02*		*0.008*		*0.064*		*0.019*		*0.04*		*0.055*		*0.075*		*0.08*	
5	*0.02*		*0.009*		*0.059*		*0.025*		*0.045*		*0.054*		*0.07*		*0.074*	
10	*0.02*		*0.01*		*0.057*		*0.025*		*0.05*		*0.052*		*0.065*		*0.071*	
20	0.0194	0.0070	0.0128	0.0018	0.0549	0.0549	0.0296	0.0085	0.0528	0.0212	0.0510	0.0067	0.0567	0.0103	0.0681	0.0091
30	0.0181	0.0049	0.0208	0.0025	0.0455	0.0455	0.0423	0.0094	0.0727	0.0094	0.0391	0.0072	0.0628	0.0084	0.0637	0.0082
40	0.0209	0.0098	0.0245	0.0030	0.0565	0.0565	0.0613	0.0077	0.0732	0.0179	0.0476	0.0054	0.0390	0.0075	0.0591	0.0080
50	0.0225	0.0069	0.0274	0.0033	0.0568	0.0568	0.0795	0.0252	0.0738	0.0184	0.0656	0.0048	0.0393	0.0137	0.0562	0.0074
60	0.0169	0.0060	0.0318	0.0038	0.0597	0.0597	0.0795	0.0137	0.0857	0.0137	0.0703	0.0070	0.0720	0.0098	0.0611	0.0078
70	0.0193	0.0054	0.0368	0.0059	0.0784	0.0784	0.0973	0.0124	0.0908	0.0122	0.0687	0.0057	0.0846	0.0160	0.0722	0.0093
80	0.0174	0.0034	0.0465	0.0058	0.0950	0.0950	0.0950	0.0123	0.101	0.013	0.0939	0.0088	0.083	0.014	0.0909	0.0126
90	0.0226	0.0049	0.0510	0.0066	0.118	0.118	0.110	0.017	0.114	0.021	0.095	0.010	0.108	0.020	0.091	0.011
100	0.0263	0.0034	0.0638	0.0089	0.144	0.144	0.146	0.027	0.142	0.019	0.122	0.011	0.102	0.013	0.111	0.014
110	0.0270	0.0033	0.0839	0.0109	0.144	0.144	0.132	0.019	0.158	0.018	0.134	0.012	0.151	0.021	0.127	0.016
120	0.0337	0.0046	0.0985	0.0118	0.158	0.158	0.147	0.019	0.176	0.021	0.146	0.021	0.155	0.019	0.144	0.021
130	0.0354	0.0055	0.1079	0.0140	0.183	0.183	0.180	0.026	0.198	0.041	0.179	0.018	0.168	0.024	0.158	0.026
140	*0.04*		*0.11*		*0.2*		*0.21*		*0.2*		*0.2*		*0.18*		*0.165*	
150	*0.045*		*0.13*		*0.21*		*0.25*		*0.22*		*0.21*		*0.195*		*0.175*	
160	*0.048*		*0.15*		*0.22*		*0.28*		*0.25*		*0.22*		*0.2*		*0.185*	
170	*0.052*		*0.155*		*0.23*		*0.29*		*0.28*		*0.24*		*0.215*		*0.19*	
180	*0.055*		*0.16*		*0.24*		*0.32*		*0.32*		*0.25*		*0.23*		*0.2*	
ICS	0.334	0.067	0.809	0.067	1.51	0.24	1.58	0.26	1.66	0.27	1.43	0.23	1.40	0.23	1.34	0.22
MTCS	0.393	0.076	1.08	0.09	1.91	0.30	2.01	0.31	2.05	0.32	1.82	0.28	1.76	0.27	1.63	0.25
E_0 (eV)→	14 eV		14.5 eV		15 eV		15.5 eV		16 eV		17.5 eV		20 eV		25 eV	
Angle (deg)↓	DCS	Error	DCS	Error	DCS	Error	DCS	Error	DCS	Error	DCS	Error	DCS	Error	DCS	Error
0	*0.1*		*0.1*		*0.13*		*0.095*		*0.105*		*0.14*		*0.076*		*0.08*	
5	*0.09*		*0.09*		*0.1*		*0.093*		*0.105*		*0.14*		*0.076*		*0.075*	
10	*0.085*		*0.085*		*0.09*		*0.09*		*0.0975*		*0.13*		*0.076*		*0.07*	
20	0.0758	0.0128	0.0747	0.0093	0.0760	0.0196	0.0773	0.0120	0.0911	0.0131	0.0944	0.0135	0.0683	0.0231	0.0627	0.0127
30	0.0659	0.0160	0.0702	0.0104	0.0646	0.0100	0.0769	0.0153	0.0751	0.0174	0.0687	0.0102	0.0618	0.0076	0.0726	0.0137
40	0.0649	0.0127	0.0663	0.0098	0.0588	0.0116	0.0807	0.0106	0.0785	0.0112	0.0649	0.0106	0.0683	0.0085	0.0591	0.0142
50	0.0579	0.0089	0.0657	0.0109	0.0629	0.0076	0.0656	0.0084	0.0626	0.0113	0.0593	0.0090	0.0589	0.0071	0.0482	0.0072
60	0.0604	0.0078	0.0816	0.0117	0.0631	0.0107	0.0706	0.0103	0.0594	0.0095	0.0551	0.0095	0.0543	0.0077	0.0532	0.0066
70	0.0649	0.0083	0.0749	0.0116	0.0586	0.0100	0.0595	0.0104	0.0618	0.0118	0.0520	0.0067	0.0524	0.0075	0.0400	0.0049
80	0.0812	0.0102	0.0890	0.0123	0.0704	0.0122	0.0703	0.0097	0.0694	0.0084	0.0547	0.0093	0.0557	0.0071	0.0415	0.0054
90	0.0819	0.0105	0.0996	0.0127	0.0732	0.0088	0.0771	0.0114	0.0620	0.0111	0.0554	0.0070	0.0584	0.0089	0.0381	0.0046
100	0.102	0.014	0.0966	0.0195	0.0836	0.0117	0.0939	0.0145	0.0811	0.0102	0.0630	0.0113	0.0615	0.0076	0.0348	0.0048
110	0.113	0.015	0.107	0.018	0.0999	0.0121	0.101	0.013	0.0884	0.0106	0.0837	0.0105	0.0675	0.0109	0.0312	0.0037
120	0.124	0.019	0.125	0.028	0.118	0.015	0.107	0.014	0.105	0.013	0.0924	0.0117	0.0697	0.0085	0.0340	0.0041
130	0.140	0.018	0.158	0.024	0.128	0.017	0.116	0.018	0.116	0.026	0.0949	0.0130	0.0647	0.0080	0.0397	0.0048
140	*0.16*		*0.18*		*0.18*		*0.14*		*0.113*		*0.1*		*0.07*		*0.043*	
150	*0.17*		*0.19*		*0.2*		*0.155*		*0.124*		*0.11*		*0.072*		*0.047*	
160	*0.18*		*0.21*		*0.23*		*0.158*		*0.12*		*0.11*		*0.072*		*0.05*	
170	*0.185*		*0.22*		*0.25*		*0.16*		*0.12*		*0.11*		*0.072*		*0.052*	
180	*0.2*		*0.23*		*0.28*		*0.165*		*0.12*		*0.11*		*0.072*		*0.055*	
ICS	1.25	0.20	1.37	0.23	1.24	0.19	1.17	0.18	1.06	0.17	0.938	0.147	0.790	0.124	0.559	0.085
MTCS	1.50	0.24	1.64	0.27	1.54	0.23	1.35	0.20	1.18	0.18	1.03	0.16	0.813	0.124	0.512	0.076

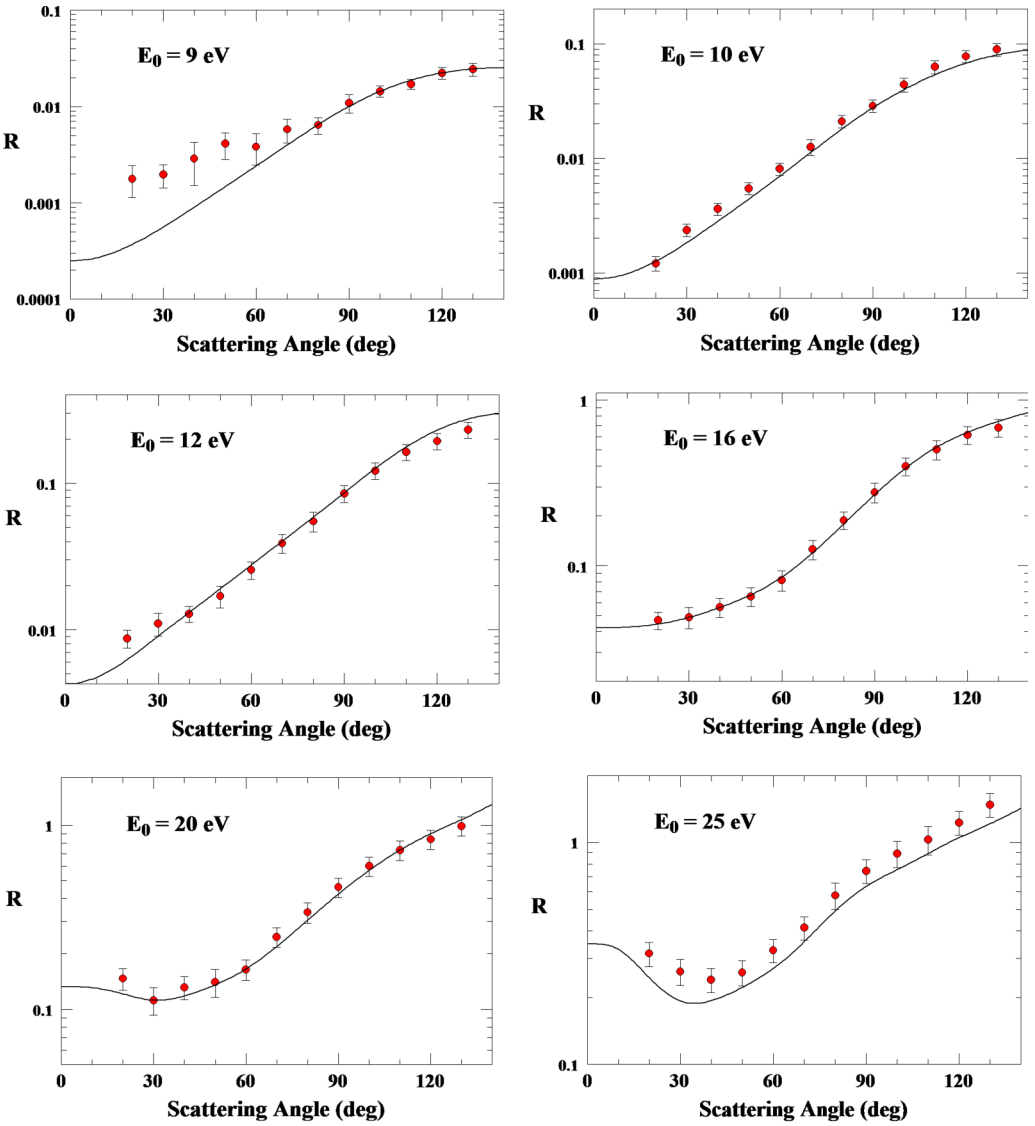

FIG. 3. Selected electron-impact inelastic to elastic scattering ratios (R) from the experimental TOF spectra (●) and compared with the present CCC results (—). See text for discussion.

measurements of R, with B fields of about 30–40 mG, showed poor agreement with the CCC results. When the B fields in the chamber were reduced to $<\pm 2$ mG the system began to take meaningful R values. At E_0 values above 16 eV, R values were found to be in excellent agreement with the theory within error bars of about 8%–15%, but at E_0 values of $\leqslant 10$ eV we see some disagreement, especially at 9 eV where we observe a more leveling trend of R with significantly increased errors, suggesting a possible limit to the operation of the present experimental apparatus, although we have reproduced these R values with different experimental conditions (e.g., focusing voltages of F2, see Fig. 1). At higher E_0 values excellent agreement is observed. When E_0 is significantly above the ionization potential of 15.43 eV; i.e., at 17.5, 20, and 25 eV, the observed R values begin to exceed the CCC R values. This is easily visible at $E_0 = 25$ eV. This is due to the detector now also picking up ionized ejected electrons in addition to scattered electrons, which then add to the total inelastically detected electrons. A method to approximately reconcile the measured R ratios with those of the CCC is addressed in detail further in Sec. IV E since the accuracy of experimental elastic electron scattering DCSs employed (for normalizing our TOF spectra) was central to obtaining accurate experimental inelastic DCSs; this is discussed next.

C. Elastic scattering DCSs used for normalization of inelastic DCSs

The experimental elastic electron scattering DCSs, used to normalize the TOF spectra intensities, were taken by our group in 2008 [29] with the movable aperture source method [44], which has been well tested in our laboratory [59]. These are fundamental to our present quantitative DCSs for excitation of H_2 so a brief discussion of these is made here. The elastic DCSs used were obtained at all E_0 values in this work from 9 to 20 eV either directly or interpolated. However, the elastic scattering DCSs from [29] were available only up to $E_0 = 20$ eV, and so we interpolated these elastic

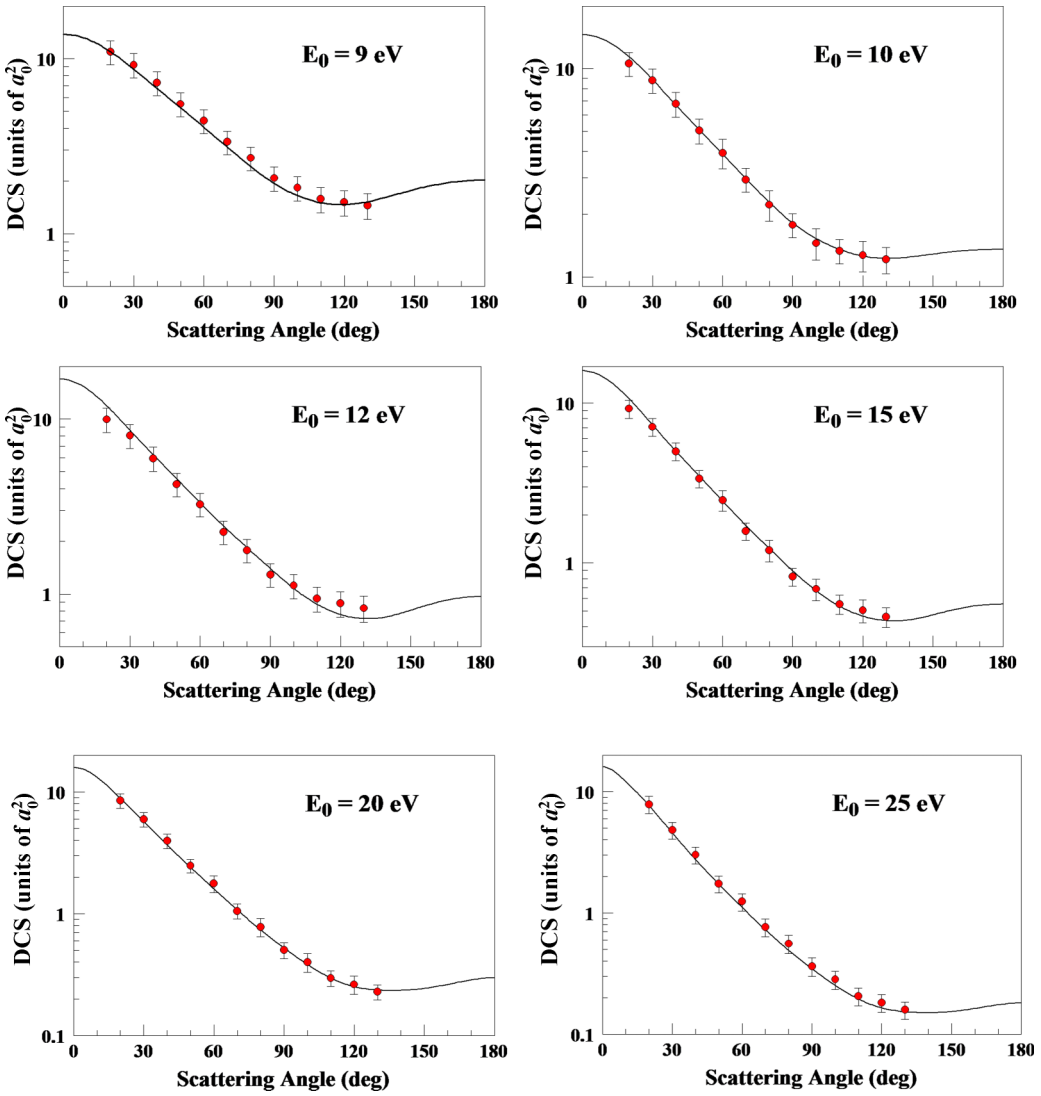

FIG. 4. Electron-impact elastic scattering DCS values (in atomic units) used in the present experimental work which were used to normalize the inelastic features of our TOF spectra compared to CCC. Legend is the same as Fig. 3. The measured DCSs at 9–20 eV are from or interpolated from [29] and those at $E_0 = 30$ eV are an interpolation of these DCSs and those of [28] at $E_0 = 30$ eV. See text for discussion.

DCSs further above $E_0 = 20$ eV using the $E_0 = 30$ eV DCSs of Khakoo and Trajmar [28] which allowed us to extend the empirical experimental elastic DCSs used here to $E_0 = 25$ eV. The overall agreement with the present CCC was found to be excellent as is shown in Fig. 4, and enabled us to convert our R values in Table I to accurate DCSs for various features in the inelastic TOF spectra.

D. DCSs for the excitation of the $X\,^1\Sigma_g{}^+ \rightarrow b\,^3\Sigma_u{}^+$ transition

We note that for $E_0 < 11$ eV, i.e., below the threshold for exciting the lowest, bound $B\,^1\Sigma_u{}^+$ electronic states of H_2, only the $X\,^1\Sigma_g{}^+ \rightarrow b\,^3\Sigma_u{}^+$ transition is excited. Selected experimental DCSs for excitation of the $X\,^1\Sigma_g{}^+ \rightarrow b\,^3\Sigma_u{}^+$ transition (see also Table I) are plotted against the CCC results in Fig. 5. Here we also compare with available electron energy-loss spectroscopy measurements. Again, as with the R values, we see excellent agreement with the CCC results for $E_0 \geqslant 10$ eV. At the lowest E_0 values of 9 eV (as for R) we find disagreement with the theory at $\theta \leqslant 70°$. However, the CCC curve is in excellent agreement with the $b\,^3\Sigma_u{}^+$ excitation DCSs of [24] taken with an electrostatic electron spectrometer. We note that at $E_0 = 9$ eV the CCC and our elastic scattering DCSs from [29], on which the present normalizations are based, show perfect agreement; this confines the problem to the inelastic $b\,^3\Sigma_u{}^+$ state excitation. We have reproduced the present DCSs at 9 eV with different focusing of the electron beam and so are presently not sure of any systematic problems with these experimental DCSs at small θ which could cause them to be at variance with CCC. Certainly the fact that the theory agrees well with the experimental DCSs of [24] is not a full affirmation that the experimental DCSs at this energy from [24] are accurate. The discrepancy between the CCC results and the present DCS measurements at 9.0 eV may result from the limitation of the AN approximation in accurately modeling the nuclear dynamics at low incident energies. At $E_0 = 10$ eV agreement with the CCC theory is improved, and our DCSs are found to be in very

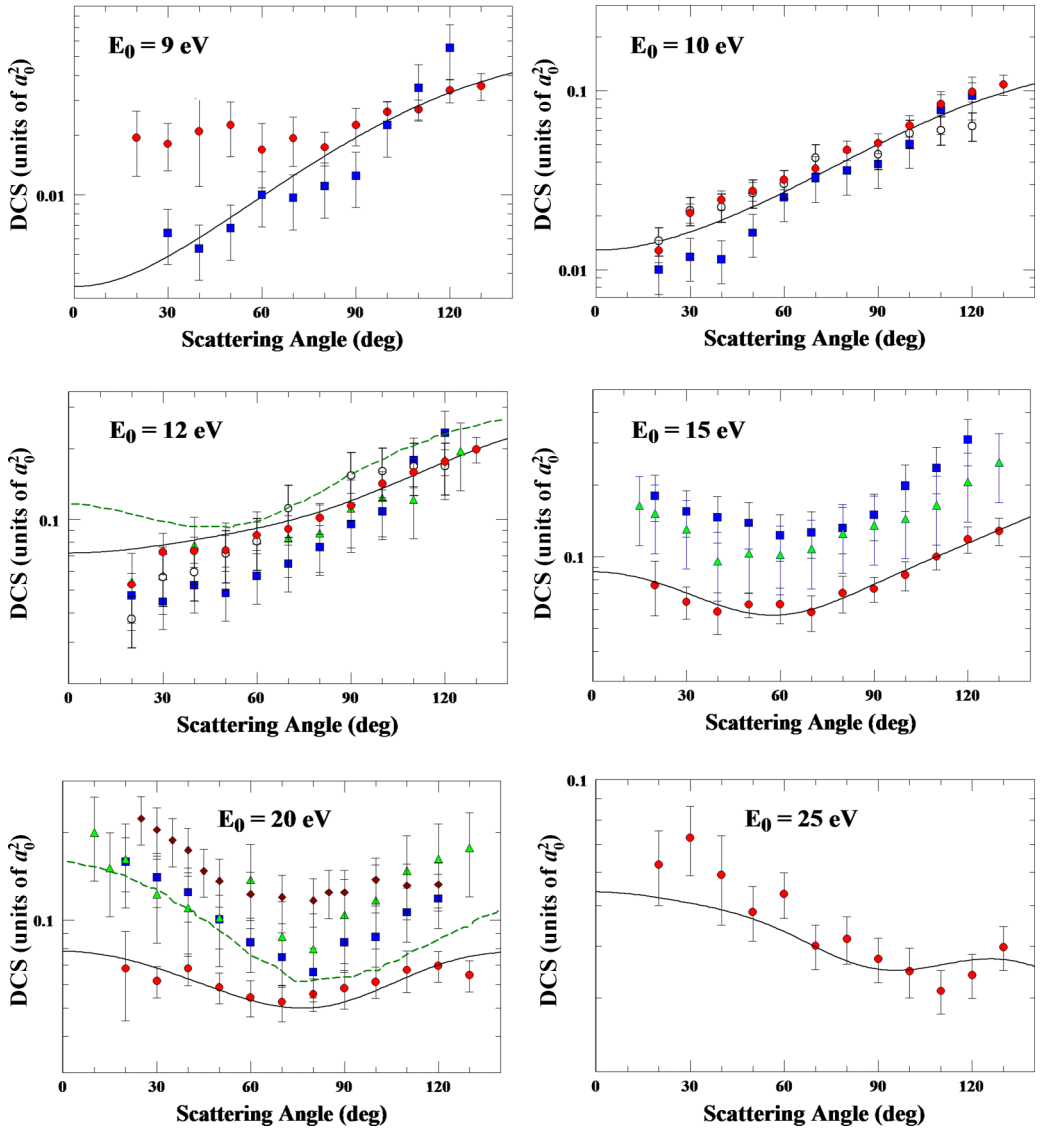

FIG. 5. Selected electron-impact excitation scattering DCS values (in atomic units) for exciting the $X\,^1\Sigma_g{}^+ \rightarrow b\,^3\Sigma_u{}^+$ transition. Legend is as in Fig. 3, and (○) Hall and Andric [21]; (▲) Nishimura and Danjo [22]; (♦) Khakoo *et al.* [23]; (■) Khakoo and Segura [24]; (---) da Costa *et al.* SMC model [9].

good agreement with the available results of Hall and Andric [21], with both being somewhat higher than the present CCC theory. Here the earlier measurements of [24] are lower than the present measurements and [21] and the CCC theory for $\theta \leqslant 50^\circ$. At $E_0 = 12$ eV, agreement with the CCC results and measurements of [21,27] is very good. The DCSs from [24] are significantly lower. At $E_0 = 12$ eV, the SMC model of [9] shows a forward rise for $\theta > 40^\circ$, which is not observed in the CCC and experimental DCSs. At higher E_0 values agreement between the present measurements and CCC is excellent. For example, here, at $E_0 = 15$ and 20 eV, the results of [22,23] plus those of [24] are significantly higher than the CCC results, which are in excellent agreement with the present TOF DCSs. We note that all the DCS angular distributions stay in very good agreement with each other, but differ in magnitude. At 20 eV, the SMC model [9] shows a larger forward peaking than the CCC calculations and the present experiment. However, it agrees very well with an earlier experiment [24]. At 25 eV, excellent agreement between the present measurements and CCC is observed.

E. DCSs for total inelastic (excitation plus ionization) scattering from H_2

In Fig. 6 we plot the total inelastic DCSs which are obtained from our R values and the elastic scattering H_2 DCSs. However, above the ionization potential (at the E_0 values of 17.5, 20, and 25 eV shown here) our TOF detector detects the ionized electron additionally to the inelastically scattered projectile electron. To approximately account for the signal of electrons in the ionization continuum range we have divided this ionization signal by 2 and added it to the electronic state inelastic scattering intensity (see, e.g., [33] where this factor of 2 arises). An example of such a spectrum is shown in Fig. 2(d), where the ionization continuum is visible. This allows us to make a more meaningful comparison with the

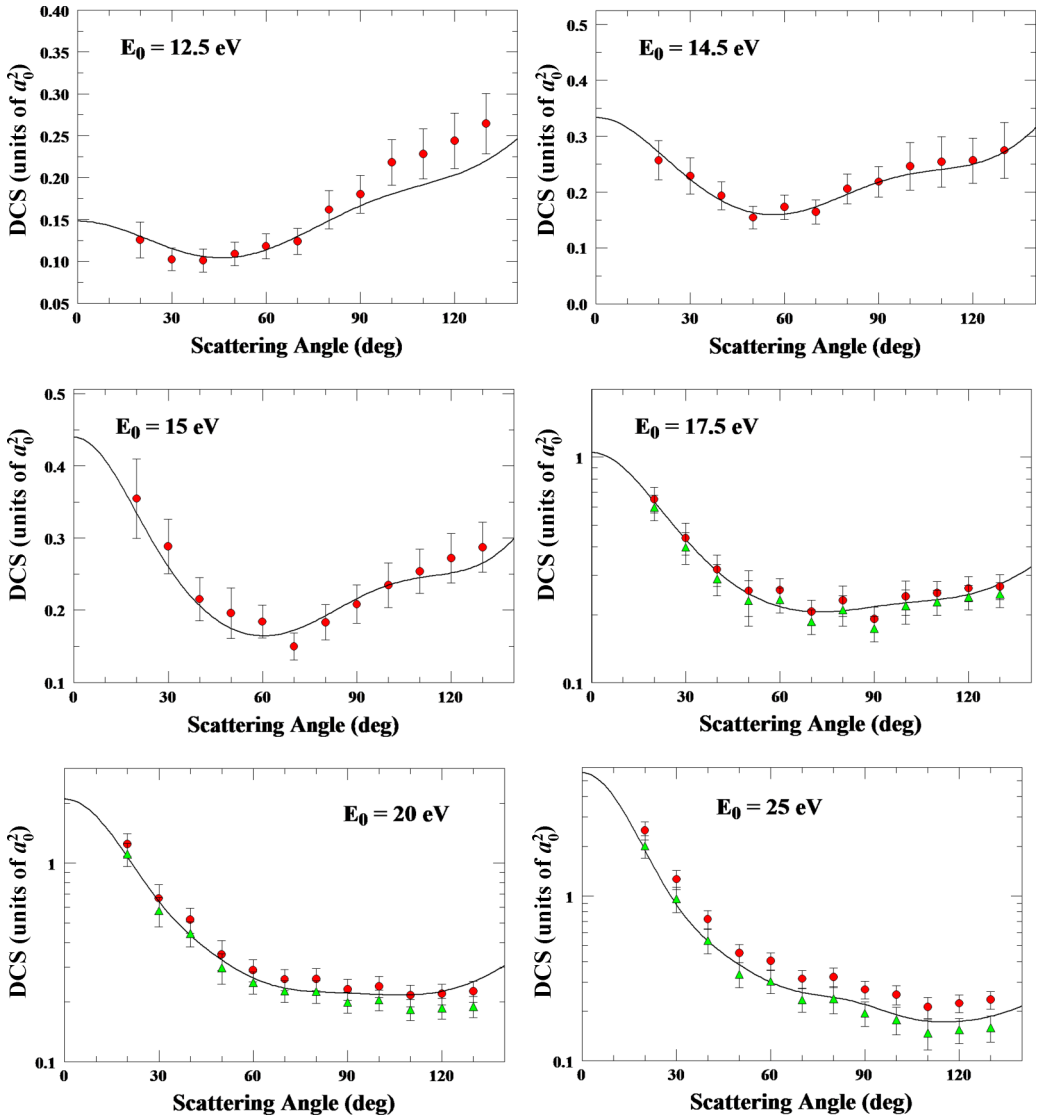

FIG. 6. Selected electron-impact total inelastic scattering (excitation plus ionization) DCS values (in atomic units) for H_2. The present experimental results from the full TOF spectral intensities (●) are corrected by adding half of the ionization intensity from the TOF spectra, to get more meaningful agreement (▲) with the CCC results line. See text for discussion.

CCC theory and is discussed also for comparing our ionization DCSs with those of the CCC in the next section, Sec. IV F. At essentially all E_0 values agreement with the CCC is excellent. At $E_0 = 12.5$ eV we do not observe the oscillations showed by the CCC, but they are in very good quantitative agreement. The ionization-corrected DCSs at $E_0 \geqslant 17.5$ eV also show excellent agreement with the CCC.

F. DCS for ionization at E_0 significantly above the ionization potential

The fully differential ionization cross sections of H_2 have been studied both theoretically and experimentally [60–63]. In Fig. 7 we plot the differential ionization cross section at E_0 of 17.5, 20, and 25 eV obtained by integrating the TOF spectrum above the 15.4-eV ionization threshold TOF and dividing this by 2, since we observed that our integrated counts were interestingly a factor of roughly 2 higher than the CCC ionization DCS. If we scaled our measurements down by a factor of 2, the agreement improved greatly and we were able to get very good agreement with the CCC results. The explanation is that at any given θ our TOF detector picks up both the scattered electron as well as the ionized electron. The angular distributions of these two must be approximately similar and simply add up to twice the scattered signal. One should be careful to realize that that this is only a very approximate correction, as can be gauged from the disagreement at $E_0 = 17.5$ eV around $\theta = 60°$, whereas for $E_0 = 20$ eV the disagreement is in the backward scattering of $\theta \geqslant 90°$. This likely indicates that the angular distributions of the scattered and ejected electrons differ significantly at $E_0 = 17.5$ and 20 eV, but not as much at 25 eV. Certainly in the forward direction, the angular distributions of the scattered and ionized electrons match very well in magnitude. However, at low excess energies above the ionization threshold postcollision interactions (PCIs) between the outgoing electrons are strong and the ejected electron is emitted in the opposite direction to the scattered electron. If the slower electron is scattered in the backward direction

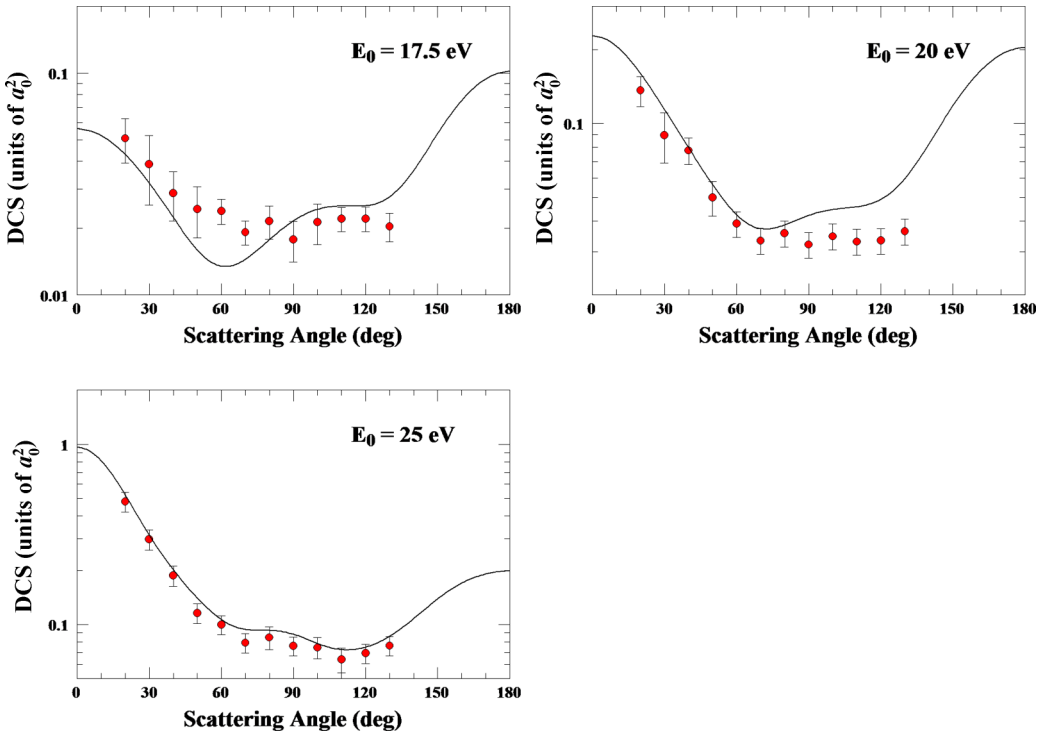

FIG. 7. Selected electron-impact ionization DCS values (in atomic units) for ionizing H_2. Legend is the same as Fig. 3. The measured ionization signal to obtain the ionization DCS (via normalization to the elastic scattering DCSs of [28,29]) has been divided by 2. See text for discussion.

(seeing the forward peak in the scattering representing the projectile electron), a large backward scattering results, i.e., almost twice the forward peak as is shown by the CCC results at $E_0 = 17.5$ eV, but this is unfortunately not covered by the experiment because of geometry constraints (see Fig. 1). As the excess energy above ionization is increased at increased E_0, PCI effects will lessen and we see an ongoing rapid decrease in the backward scattering as E_0 is raised up to 20 and 25 eV as compared to at 17.5 eV. As aforementioned the fact that we detect both electrons will raise the experimental R values for TOF spectra taken above the ionization potential, and this will get more pronounced at higher E_0 above the ionization potential as is easily evident at $E_0 = 25$ eV. Preliminary, but unanalyzed, measurements at $E_0 = 30$ eV show that R is even more raised from the CCC curve, but these results are not presented here, because the $X\,^1\Sigma_g{}^+ \rightarrow b\,^3\Sigma_u{}^+$ feature is smaller and more compressed in the TOF spectrum, making it difficult to analyze. The increased R values can be expected as the ionization cross section increases significantly over the excitation cross section at these higher E_0 values, where we note that the total ionization cross section peaks at approximately 65 eV [16], and spin-exchange excitation cross sections rapidly decrease from their peak cross section with respect to increasing E_0, making the $X\,^1\Sigma_g{}^+ \rightarrow b\,^3\Sigma_u{}^+$ TOF feature weaker and increasingly difficult to analyze.

G. ICSs for the excitation of the $X\,^1\Sigma_g{}^+ \rightarrow b\,^3\Sigma_u{}^+$ transition

Figure 8 shows the ICSs obtained by extrapolating the b-state excitation DCSs to small and large θ and integrating these DCSs with respect to the solid angle $d\Omega$ in a standard procedure. For the ICSs, excellent agreement is observed with the CCC results at all E_0 values. We note that for $E_0 > 12$ eV, the earlier energy-loss measurements are significantly higher, especially at $E_0 = 15$ eV. Underdetermining the background for the continuum is a likely cause of this since the $X\,^1\Sigma_g{}^+ \rightarrow b\,^3\Sigma_u{}^+$ transition extends further than the energy-loss value of 16 eV. Above the energy loss of

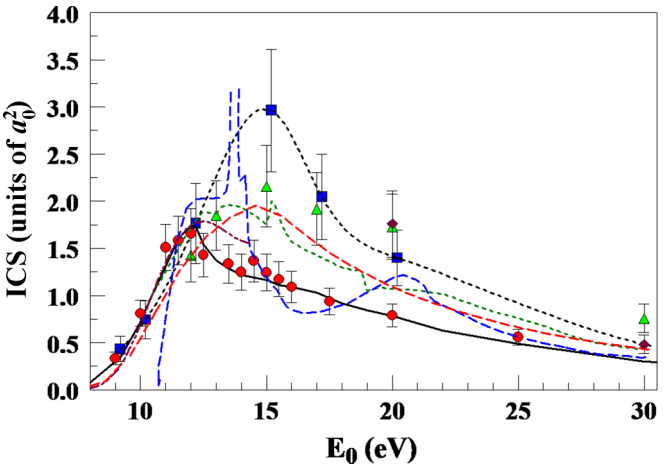

FIG. 8. ICSs in atomic units for excitation of the $b\,^3\Sigma_u{}^+$ state at various E_0 values. Legend is the same as for Figs. 3 and 5 except (— —) Gorfinkiel and Tennyson [8]; (— - - —) Trevisan and Tennyson [56]; (- — — —) Celiberto *et al.* [64]. The recommended ICSs by Yoon *et al.* [7] (-----) are the ICSs of [24] from 9.2 to 20 eV and ICSs of [23] from 30 to 100 eV.

16 eV it overlaps with transitions to the upper bound states $X\,^1\Sigma_g{}^+ \rightarrow B\,^1\Sigma_u{}^+$, $c\,^3\Pi_u$, $a\,^3\Sigma_g{}^+$, $C\,^1\Pi_u$, and $E(F)\,^1\Sigma_g{}^+$. This will add intensity to the (extended) $X\,^1\Sigma_g{}^+ \rightarrow b\,^3\Sigma_u{}^+$ continuum energy loss. The CCC calculations demonstrate that above $E_0 = 12$ eV, the higher-lying electronic states (e.g., the $B\,^1\Sigma_u{}^+$, $c\,^3\Pi_u$, $a\,^3\Sigma_g{}^+$, $C\,^1\Pi_u$, and $E(F)\,^1\Sigma_g{}^+$ states) couple strongly to the $b\,^3\Sigma_u{}^+$ continuum and cause the cross section for excitation of the $b\,^3\Sigma_u{}^+$ state to be reduced dramatically, as can be seen in Fig. 8. Only in a multistate close-coupling model would the effect of such interchannel interactions be properly modeled or even detectable, and this demonstrates the significant advantage of close-coupling models over perturbative models in terms of the type of physics that they bring into the electron-scattering dynamics. We also plot the latest values of the FN models, viz., the SMC model of da Costa *et al.* [9] and the *R*-matrix model of Gorfinkiel and Tennyson [8] plus the AN models, viz., the energy-balanced model of Trevisan and Tennyson [56] and the semiclassical AN Gryzinski approximation of Celiberto *et al.* [64]. Gorfinkiel and Tennyson [8] observe strong peaks around $E_0 = 13.7$ to 13.9 eV due to two strong and sharp H_2^- resonances in the $^2\Sigma_g{}^+$ and $^2\Sigma_u{}^+$ partial waves, which are not detected in the present experiment. Similar resonances are seen in the FN CCC cross sections, but they are not present in the AN results after averaging over the initial vibrational wave function (see Ref. [18]). The FN results of [9] show excellent agreement between 10 and 12 eV, but do not reproduce the drop in ICS at higher energies. At low incident energies, the FN approximation breaks down and it is necessary to account for the nuclear dynamics of the molecule by implementing the AN method. We have confirmed previously [18] that the FN approximation is valid only above 14 eV for excitation of the $b\,^3\Sigma_u{}^+$ state. The AN *R*-matrix calculation of [56] agrees well with the present theory and experiment between 10 and 12 eV, but is overestimated at higher energies due to the small (nine-state) close-coupling expansion utilized. Below 10 eV the results of [56] are lower than the AN CCC curve due to their use of an energy-balancing technique which aims to correct the violation of energy conservation in the AN approximation at near-threshold energies. It has been confirmed that the AN CCC results are in agreement with [56] when the energy-balancing technique is implemented; however, the standard AN method presented in Fig. 8 yields better agreement with the present ICS measurements. The ICS values of the AN Gryzinski method [64] are found to be significantly larger than the present measurements and CCC calculations above approximately 12 eV. Finally, similar to the CCC method, the *R*-matrix calculations also observe the interchannel coupling effects which significantly reduce the ICSs around $E_0 = 14$ eV, and again demonstrate the physical importance of close-coupling models to detect such interchannel coupling. Aside from the CCC calculations for scattering on H_2 and $H_2{}^+$, no other theoretical treatments of electron-molecule scattering have provided detailed convergence studies. It is worth noting that without demonstration of convergence in theoretical cross sections, agreement with experiments may be deceiving. For example, the two-state close-coupling calculations of Rescigno and Schneider [65] for the $X\,^1\Sigma_g{}^+ \rightarrow b\,^3\Sigma_u{}^+$ transition are in excellent agreement with the measurements of [22]; however, it has now been shown that in this case both the experimental and theoretical values were significantly overestimated. The results of the present study emphasize the importance of performing convergence studies as developments in computational methods and resources allow large-scale close-coupling calculations to be performed for more complex molecules.

V. CONCLUSIONS

The present work presents inelastic to elastic *R* ratios for electron scattering from H_2 for E_0 from 9 to 25 eV. These *R* values are used to obtain normalized inelastic scattering DCSs for excitation of the summed states of H_2 by normalization of elastic scattering DCSs of [28,29] to obtain inelastic DCSs. Additionally, unfolding the TOF spectrum for the partially exposed low-lying $X\,^1\Sigma_g{}^+ \rightarrow b\,^3\Sigma_u{}^+$ transition in H_2 enabled us to obtain DCSs for exciting the $b\,^3\Sigma_u{}^+$ state. These measurements were motivated by the progress in the theoretical modeling of e^--H_2 collisions in the CCC model and significant disagreements found by it with previous experimental data for the $X\,^1\Sigma_g{}^+ \rightarrow b\,^3\Sigma_u{}^+$ transition. A TOF machine was built that does not suffer the problems typical for previous measurements based on electrostatic spectrometers. Comparisons of the scattering DCSs between the present TOF measurements and the CCC calculations show excellent agreement over a wide E_0 and θ range. ICSs for exciting the $b\,^3\Sigma_u{}^+$ state show perfect agreement with CCC. Both the CCC calculations and the present measurements observe the reduction of the $b\,^3\Sigma_u{}^+$ state excitation at $E_0 > 12$ eV due to strong interchannel coupling to other excited states that become open at these energies. We also demonstrate the use of a unique differential TOF spectrometer, which uses a lens-pulsed high-current electron gun and a compact TOF tube, for measuring accurate inelastic to elastic ratios. We intend to extend the present work to possibly other atomic and molecular targets, e.g., Kr, Xe, CO, O_2, N_2, and H_2O, in the future.

ACKNOWLEDGMENTS

M.Z. acknowledges support from the Fulbright Fellowship program. This experimental work was supported by the U.S. National Science Foundation Research in an Undergraduate Institution program under Grant No. RUI-PHY-1606905 to M.A.K. The theoretical work was supported by the United States Air Force Office of Scientific Research, Los Alamos National Laboratory (LANL) and Curtin University. L.H.S. acknowledges the contribution of an Australian Government Research Training Program Scholarship and the support of the Forrest Research Foundation. M.C.Z. would like to specifically acknowledge LANLs ASC PEM Atomic Physics Project for its support. LANL is operated by Triad National Security, LLC, for the National Nuclear Security Administration of the U.S. Department of Energy under Contract No. 89233218NCA000001. Resources were provided by the Pawsey Supercomputing Centre with funding from the Australian government and the government of Western Australia.

[1] J. P. Boeuf, G. J. M. Hagelaar, P. Sarrailh, G. Fubiani and N. Kohen, Plasma Sources Sci. Technol. **20**, 015002 (2016).
[2] Y. Ju and W. Sun, Prog. Energy Combust. Sci. **48**, 21 (2015).
[3] N. Yoshida, Astrophys. J. **663**, 687 (2007).
[4] G. J. Ferland, A. C. Fabian, N. A. Hatch, R. M. Johnstone, R. L. Porter, P. A. M. van Hoof, and R. J. R. Williams, Mon. Not. R. Astron. Soc. **392**, 1475 (2009).
[5] M. L. Lykins, G. J. Ferland, R. Kisielius, M. Chatzikos, R. L. Porter, P. A. M. van Hoof, R. J. R. Williams, F. P. Keenan, and P. C. Stancil, Astrophys. J. **807**, 118 (2015).
[6] H. Tawara, Y. Itikawa, H. Nishimura, and M. Yoshino, J. Phys. Chem. Ref. Data **19**, 617 (1990).
[7] J.-S. Yoon, M.-Y. Song, J.-M. Han, S. H. Hwang, W.-S. Chang, B. J. Lee, and Y. Itikawa, J. Phys. Chem. Ref. Data **37**, 913 (2008).
[8] J. D. Gorfinkiel and J. Tennyson, J. Phys. B **38**, 1607 (2005).
[9] R. F. da Costa, F. J. da Paixão, and M. A. P. Lima, J. Phys. B **38**, 4363 (2005).
[10] M. Tashiro and K. Morokuma, Phys. Rev. A **75**, 012720 (2007).
[11] L. Hargreaves, K. Ralphs, G. Serna, M. A. Khakoo, C. Winstead, and V. McKoy, J. Phys. B **45**, 201001 (2012).
[12] A. Loupas, K. Regeta, M. Allan, and J. D. Gorfinkiel, J. Phys. Chem. A **122**, 1146 (2018).
[13] M. C. Zammit, D. V. Fursa, and I. Bray, Phys. Rev. A **90**, 022711 (2014).
[14] I. Bray, I. B. Abdurakhmanov, J. J. Bailey, A. W. Bray, D. V. Fursa, A. S. Kadyrov, C. M. Rawlins, J. S. Savage, A. T. Stelbovics, and M. C. Zammit, J. Phys. B **50**, 202001 (2017).
[15] M. C. Zammit, D. V. Fursa, J. S. Savage, and I. Bray, J. Phys. B **50**, 123001 (2017).
[16] M. C. Zammit, J. S. Savage, D. V. Fursa, and I. Bray, Phys. Rev. Lett. **116**, 233201 (2016).
[17] M. C. Zammit, J. S. Savage, D. V. Fursa, and I. Bray, Phys. Rev. A **95**, 022708 (2017).
[18] L. H. Scarlett, J. K. Tapley, D. V. Fursa, M. C. Zammit, J. S. Savage, and I. Bray, Phys. Rev. A **96**, 062708 (2017).
[19] S. J. B. Corrigan, J. Chem. Phys. **43**, 4381 (1965).
[20] L. H. Scarlett, J. K. Tapley, D. V. Fursa, M. C. Zammit, J. S. Savage, and I. Bray, Euro. J. Phys. D **72**, 34 (2018).
[21] R. I. Hall and L. Andric, J. Phys. B **17**, 3815 (1984).
[22] H. Nishimura and A. Danjo, J. Phys. Soc. Jpn. **55**, 3031 (1986).
[23] M. A. Khakoo, S. Trajmar, R. McAdams, and T. Shyn, Phys. Rev. A **35**, 2832 (1987).
[24] M. A. Khakoo and J. Segura, J. Phys. B **27**, 2355 (1994).
[25] S. K. Srivastava, A. Chutjian, and S. Trajmar, J. Chem. Phys. **63**, 2659 (1975).
[26] S. Trajmar, D. F. Register, and A. Chutjian, Phys. Rep. **97**, 219 (1983).
[27] H. Nishimura, A. Danjo, and H. Sugahara, J. Phys. Soc. Jpn. **54**, 1757 (1985).
[28] M. A. Khakoo and S. Trajmar, Phys. Rev. A **34**, 138 (1986).
[29] J. Muse, H. Silva, M. C. A. Lopes, and M. A. Khakoo, J. Phys. B **41**, 095203 (2008).
[30] L. R. Hargreaves, S. Bhari, B. Adjari, X. Liu, R. Laher, M. Zammit, J. S. Savage, D. V. Fursa, I. Bray, and M. A. Khakoo, J. Phys. B **50**, 225203 (2017).
[31] J. Wrkich, D. Mathews, I. Kanik, S. Trajmar, and M. A. Khakoo, J. Phys. B **35**, 4695 (2002).
[32] F. Pichou, A. Huetz, G. Joyez, and M. Landau, J. Phys. B **11**, 3683 (1978).
[33] E. Schow, K. Hazlett, J. G. Childers, C. Medina, G. Vitug, I. Bray, D. V. Fursa, and M. A. Khakoo, Phys. Rev. A **72**, 062717 (2005).
[34] L. R. LeClair and S. Trajmar, J. Phys. B **29**, 5543 (1996).
[35] L. R. LeClair, S. Trajmar, M. A. Khakoo, and J. C. Nickel, Rev. Sci. Instrum. **67**, 1753 (1996).
[36] M. Lange, J. Matsumoto, A. Setiawan, R. Panajotović, J. Harrison, J. C. A. Lower, D. S. Newman, S. Mondal, and S. J. Buckman, Rev. Sci. Instrum. **79**, 043105 (2008).
[37] M. Lange, J. Matsumoto, J. Lower, S. Buckman, O. Zatsarinny, K. Bartschat, I. Bray, and D. Fursa, J. Phys. B **39**, 4179 (2006).
[38] S. Mondal, J. Lower, S. J. Buckman, R. P. McEachran, G. Garcia, O. Zatsarinny, and K. Bartschat, PMC Phys. B **2**, 3 (2009).
[39] M. A. Khakoo, O. Zatsarinny, and K. Bartschat, J. Phys. B **44**, 015201 (2016).
[40] Avtech Electrosystems Ltd., model AVR-E5-B-05, PO Box 265, Ogdensburg, NY 13669, USA.
[41] Pasternack Enterprises, Inc., 17802 Fitch, Irvine, CA 92614, USA.
[42] Smiths Microwave, http://emc-rflabs.com, ACETEC, 6540 Lusk Blvd # C146, San Diego, CA 92121. Part #: 32-1637.
[43] ARi Industries Inc., Addison, IL 60101, USA, 1HN040B-16.3 biaxial cable.
[44] M. Hughes, K. E. James, Jr., J. G. Childers, and M. A. Khakoo, Meas. Sci. Technol. **14**, 841 (1994).
[45] Z-stack, APD 3 MA 25/12/10/12 D 60:1, PHOTONIS USA, Inc., 660 Main Street, PO Box 1659, Sturbridge, MA 01566, USA.
[46] Unique Wire Weaving, 762 Ramsey Ave, Hillside, NJ 07205, USA: 10×10 meshes/inch, 0.005 in. wire diameter.
[47] Co-netic, Magnetic Shield Corporation, Perfection Mica Company, Bensenville, IL 60106, USA.
[48] C. Chung, C. C. Lin, and T. P. Lee, Phys. Rev. A **12**, 1340 (1975).
[49] T. N. Rescigno, C. W. McCurdy, Jr., V. McKoy, and C. F. Bender, Phys. Rev. A **13**, 216 (1976).
[50] C. Chung and C. C. Lin, Phys. Rev. A **21**, 1075 (1980).
[51] A. W. Fliflet and V. McKoy, Phys. Rev. A **21**, 1863 (1980).
[52] M. A. P. Lima, T. L. Gibson, W. Huo, and V. McKoy, J. Phys. B **18**, L865 (1988).
[53] S. E. Branchett, J. Tennyson, and L. A. Morgan, J. Phys. B **23**, 4625 (1990).
[54] K. L. Baluja, C. J. Noble, and J. Tennyson, J. Phys. B **18**, L851 (1985).
[55] B. I. Schneider and L. A. Collins, J. Phys. B **18**, L857 (1985).
[56] C. S. Trevisan and J. Tennyson, J. Phys. B **34**, 2935 (2001).
[57] J. Liu, E. J. Salumbides, U. Hollenstein, J. C. J. Koelemeij, K. S. E. Eikema, W. Ubachs, and F. Merkt, J. Chem. Phys. **130**, 174306 (2009).
[58] M. Zawadzki, R. Wright, G. Dolmat, M. F. Martin, L. Hargreaves, D. V. Fursa, M. C. Zammit, L. H. Scarlett, J. K. Tapley, J. S. Savage, I. Bray, and M. A. Khakoo, Phys. Rev. A **97**, 050702(R) (2018).

[59] M. A. Khakoo, K. Keane, C. Campbell, N. Guzman, and K. Hazlett, J. Phys. B **40**, 3601 (2007).
[60] X. Ren, A. Senftleben, T. Pflüger, M. Holzwarth, A. Dorn, K. Bartschat, I. Bray, D. V. Fursa, J. Colgan, and M. S. Pindzola, J. Phys. Conf. Ser. **212**, 012003 (2012).
[61] X. Ren, A. Senftleben, T. Pflüger, A. Dorn, J. Colgan, M. S. Pindzola, O. Al-Hagan, D. H. Madison, I. Bray, D. V. Fursa, and J. Ullrich, Phys. Rev. A **82**, 032712 (2010).
[62] X. Ren, T. Pflüger, S. Xu, J. Colgan, M. S. Pindzola, A. Senftleben, J. Ullrich, and A. Dorn, Phys. Rev. Lett. **109**, 123202 (2012).
[63] J. Colgan, M. S. Pindzola, F. Robicheaux, C. Kaiser, A. J. Murray, and D. H. Madison, Phys. Rev. Lett. **101**, 233201 (2008).
[64] R. Celiberto, R. Jenev, A. Laricchuita, M. Capitelli, J. Wadehra, and D. Atems, At. Data Nucl. Data Tables **77**, 161 (2001).
[65] T. N. Rescigno and B. I. Schneider, J. Phys. B **21**, L691 (1988).